Evaluation of TiO_2/V_2O_5 and N,F-doped-TiO_2/V_2O_5 nanocomposite photocatalysts toward reduction of Cr(VI) and oxidation reactions by •OH radicals

A. Giannakas[a], F. Bairamis[b], I. Papakostas[b], T. Zerva[b], I. Konstantinou[b,*]

[a] Department of Business Administration of Agricultural and Food Enterprises, University of Patras, G. Seferi 2, Agrinio 30100, Greece
[b] Department of Chemistry, University of Ioannina, Ioannina 45110, Greece

A B S T R A C T

V_2O_5/TiO_2 photocatalysts, with V_2O_5 particles supported on TiO_2 (TV), N-TiO_2 (NTV) and N/F-TiO_2 (NFTV), were prepared with 5% wt. V_2O_5 loading and 450, 550 °C as calcination temperatures. XRD analysis showed the formation of anatase TiO_2 and very small peaks of V_2O_5. DRS UV–vis spectra showed that V_2O_5 coupling extended the absorption edge into the visible light region. Photocatalysts calcined at 450 °C exhibited higher rates of Cr(VI) reduction and •OH radical photogeneration than photocatalysts calcined at 550 °C. For catalysts at 450 °C, photocatalytic reduction of Cr(VI) follows the trend TV450 > NTV450 > NFTV450 while the •OH generation followed the reverse trend.

© 2018 The Korean Society of Industrial and Engineering Chemistry. Published by Elsevier B.V. All rights reserved.

Introduction

In the past decades titanium dioxide (TiO_2) has been extensively studied and used as a low cost and effective photocatalyst for the decomposition of various organic [1,2] and inorganic pollutants [3] in aquatic matrices. Its main disadvantages remain the absence of visible light activity due to its wide bandgap energy (E_g = 3.0–3.2 eV) and the high electron–hole recombination rate. Thus, various techniques such as metal [4] or non metal doping [5–8] and/or co doping and carbon-supported catalysts [9,10] have been employed to extend the absorption edge of solar spectrum to the visible region and reduce the recombination of electron-hole pairs, thus enhancing the photocatalytic activity of TiO_2. In addition, the coupling of TiO_2 with other semiconductors, such as WO_3/TiO_2 [11], Bi_2O_3/TiO_2 [12], Bi_2S_3/TiO_2 [13], In_2O_3/TiO_2 [14], $InVO_4/TiO_2$ [15] etc., is one more approach usually employed to extend optical absorption toward the visible part of the solar spectrum and promote charge separation.

As one of the most important metal oxide catalysts with a narrow band gap, V_2O_5 has been coupled with TiO_2 by various methods and exhibited visible-light catalytic activity [16]. The absorption spectral range of V_2O_5/TiO_2 compared with that of TiO_2 (3.0 eV, λ = 413 nm) is increased due to the small bandgap of V_2O_5 (2.2 eV, λ = 564 nm), thus the photocatalytic activity can be

extended to visible light region. In addition, V_2O_5 phase can enhance the charge separation in TiO_2 supports, thus improving the overall photocatalytic performance.

V_2O_5/TiO_2 composites are commonly used as catalysts for a number of important reactions, such as the catalytic oxidation of chlorinated benzenes [17], the DeNO$_x$ reaction [18], the partial oxidation of ethanol [19], the selective oxidation reactions of o-xylene [20], the selective reduction of NO$_x$ with NH_3 [21] as well as industrial applications including high performance cathodes for lithium ion batteries [22]. Although that V_2O_5–TiO_2 catalysts have been used in many oxidation reactions of organic air pollutants [17,19,20,23], fewer studies have been performed for their use in photocatalytic degradation of organic [24–26] and inorganic [27] pollutants in aquatic media. Recently, Isleyen et al. [25] prepared V_2O_5–TiO_2 binary oxide catalysts with different wt% V_2O_5 loading by solid-state dispersion and the nanocomposites were modified with surfactants. The evaluation of photocatalytic properties was assessed toward the degradation of 2,4-dichlorophenol (2,4-DCP) in aqueous solution under UV irradiation. It was found that 50 wt% V_2O_5–TiO_2 photocatalyst exhibited much higher photocatalytic activity than pure V_2O_5, TiO_2 and P-25 [24]. In addition, Yang et al. [26] demonstrated a facile but efficient synthesis method to V_2O_5/TiO_2 core–shell nanostructures at mild temperatures (≤100 °C). Their findings showed that the V_2O_5/TiO_2 core–shell composites showed superior sunlight photocatalytic activity compared to the pure TiO_2 nanoparticles for the degradation of organic dyes (e.g., methylene blue), probably because of the

matched energy bands between V_2O_5 and TiO_2 [26]. Finally, Xie et al. [27] prepared V_2O_5/TiO_2 nanocomposites with unique core–shell spherical nanostructures and solid sphere nanostructures by solvothermal method and hydrothermal method respectively, evaluating their photocatalytic activity toward As(III) oxidation. They concluded that V_2O_5/TiO_2 with core–shell spheres morphology exhibited an excellent photocatalytic activity in the oxidation of As (III) (about 92%), remarkably superior to the one with solid sphere nanostructure, because of its larger specific surface area, enhanced visible harvest ability and improved charge separation efficiency.

Based on the current bibliographic data, there is a lack of studies dealing with the use of V_2O_5/TiO_2 catalysts for the photocatalytic reduction of heavy metal ions in aquatic media, especially for Cr(VI), which is one of the most frequent and toxic contaminants in wastewaters arising from various industrial processes [28–32], as well as on the potential application for the simultaneous Cr(VI) reduction and oxidation of organics. In addition, the photocatalytic oxidation in aqueous phase presented also limited applications and studies while the coupling with non-metal doped TiO_2 materials has not been assayed so far. Finally, a comparative study on the photocatalytic oxidation/reduction capability of composite V_2O_5/TiO_2 catalysts is also lacking. In our previous report [6], N-TiO_2 and N/F-TiO_2 photocatalysts have been successfully prepared, characterized and applied for the photocatalytic reduction of Cr(VI) in aquatic solutions. It has been demostrated that such photocatalysts exhibited enhanced reduction ability and thus were successfully implemented in the simultaneous photocatalytic oxidation of benzoic acid and photocatalytic reduction of Cr(VI) ions [33,34].

Based on the above, this work aims to achieve three main goals: [i] the successful preparation and characterization of V_2O_5/TiO_2 photocatalysts with V_2O_5 supported on TiO_2, N-TiO_2, N,F-TiO_2 photocatalysts via a simple impregnation method, [ii] the evaluation of the prepared V_2O_5/TiO_2, V_2O_5/N-TiO_2 and V_2O_5/N,F-TiO_2 photocatalysts for reduction and oxidation reactions, and [iii] the comparison of TiO_2 vs N-TiO_2 and N,F-TiO_2 as supporting materials for V_2O_5 and their effect on the photocatalytic efficiency.

Experimental

Preparation of photocatalysts

Preparation of TiO_2, N-TiO_2 and N,F-TiO_2 substrate catalysts

TiO_2, N-TiO_2 and N,F-TiO_2, catalysts were prepared as previously reported [6] and only the final calcination temperature was changed to 400 °C. Briefly, 3.4 mL titanium(IV) *n*-butoxide was added drop wise to 50 mL aqueous solution containing 0.53 g NH_4Cl (as N source) or to 50 mL aqueous solution containing 0.37 g NH_4F (as N,F source). The so obtained milky suspensions were aged for 24 h at room temperature (25 °C) and subsequently dried at 100 °C for 48 h. The obtained xerogels were calcined at 400 °C for 1 h in air with a ramp rate of 5 °C/min.

Preparation of V_2O_5/TiO_2, V_2O_5/N-TiO_2 and V_2O_5/N,F-TiO_2 nanocomposite catalysts

One gram of the as prepared TiO_2, N-TiO_2 and N,F-TiO_2 fine powdered catalysts was suspended under vigorous stirring in 50 mL of double distilled water. Then, the appropriate amount of $NH_4V_2O_4$ (0.0643 g) was added in order to achieve a final V_2O_5 to TiO_2 loading equal to 5% wt. which is selected as optimum according to previous reports [17,27]. After vigorous stirring for 12 h at room temperature (25 °C) the suspensions were spread to petri dishes and dried at 100 °C for 24 h. The obtained powders were calcined at 450 °C or 550 °C for 1 h in air with a ramp rate of 5 °C/min. V_2O_5/TiO_2, V_2O_5/N-TiO_2 and V_2O_5/N,F-TiO_2 samples calcined at 450 °C were labeled as TV450, NTV450 and NFTV450 correspondingly, while V_2O_5/TiO_2, V_2O_5/N-TiO_2 and V_2O_5/N,F-TiO_2 samples calcined at 550 °C were labeled as TV550, NTV550 and NFTV550, respectively. The full details of the chemical conditions used for each sample, are listed in Table 1.

XRD analysis

X-ray diffraction (XRD) patterns of all obtained V_2O_5/TiO_2, V_2O_5/N-TiO_2 and V_2O_5/N,F-TiO_2 were recorded by a Brüker Advance D8 XRD instrument generating monochromated CuKa (k = 1.5418 Å) radiation with continuous scanning rate of 2° min^{-1} in the range $10° < 2\theta < 90°$. The XRD patterns were assigned using the Joint Committee on Powder Diffraction Standards (JCPDS) database and then were analyzed with Rietvield refinement using an applicable computer program.

Raman measurements

Raman spectra were collected using Ar$^+$ excitation source at 514 nm wavelength coupled with A Jobin–Yvon Horiba LabRam-HR Mirco Raman spectrometer equipped with an Olympus microscope and using a 50× objective. The laser power was 4.3 mW and the spectra were recorded with an acquisition time of 30 s.

UV–vis diffuse reflectance spectrophotometry (DRS) and Fourier-transform infra-red (FTIR) spectroscopy

FT-IR spectra of materials were recorded on a Thermo Scientific FT-IR System (Nicolet iS5). The KBr pellets were prepared by mixing the studied catalysts with KBr (Acros Organics, >99%, IR grade) at 1/5 ratio. A Shimadzu (UV-2600) UV–vis spectrophotometer equipped with IRS-2600 integration sphere was used to record the absorbance spectra of the photocatalysts in 220–800 nm wavelength range at room temperature using $BaSO_4$ as reference standard. The band gap value was estimated by extrapolating the linear part of the plot of $(F(R)h\nu)^{1/2}$ versus $h\nu$: $F(R)h\nu = A(h\nu - E_g)^2$, where $F(R) = (1 - R)^2/2R$ stands for the Kübelka–Münk function

Table 1
The compositions of sols employed for the preparation of V_2O_5/TiO_2, V_2O_5/N-TiO_2 and V_2O_5/N,F-TiO_2 photocatalysts.

Sample name	Code name	NH_4Cl (g–mol)	NH_4F (g–mol)	TBOT (mL–mol)	Total sol volume (mL)	Calcination temperature (°C)
TiO_2	–	–	–	3.4–0.01	50	400
N-TiO_2	–	0.53–0.01	–	3.4–0.01	50	400
N,F-TiO_2	–	–	0.37–0.01	3.4–0.01	50	400

Sample name	Code name	TiO_2 (g)	N-TiO_2 (g)	N,F-TiO_2 (g)	$NH_4V_2O_4$ (g)	Total %wt. V_2O_5 content	Total sol volume (mL)	Calcination temperature (°C)
V_2O_5/TiO_2	TV450	1	–	–	0.064	5	50	450
V_2O_5/N-TiO_2	NTV450	–	1	–	0.064	5	50	450
V_2O_5/N,F-TiO_2	NFTV450	–	–	1	0.064	5	50	450
V_2O_5/TiO_2	TV550	1	–	–	0.064	5	50	550
V_2O_5/N-TiO_2	NTV550	–	1	–	0.064	5	50	550
V_2O_5/N,F-TiO_2	NFTV550	–	–	1	0.064	5	50	550

calculated from the reflectance spectrum and *hv* is the photon energy expressed in eV [35,36].

Porosimetry

The specific surface area (SSA) $(m^2\,g^{-1})$, as well as the total pore volume V_{TOT} $(cm^3\,g^{-1})$, were determined by N_2 adsorption–desorption porosimetry at 77 K using Quantachrome Autosorb-1instrument. Prior to the measurement, the sample ($\cong$250 mg) was degassed for 6 h at 80 °C to eliminate any moisture and condensed volatiles. Brunauer–Emmett–Teller (BET) method was used for the determination of SSA at relative pressures between 0.05 and 0.3. The total pore volume, V_{TOT}, was determined based on the amount of nitrogen adsorbed at a relative pressure $P/P_0 = 0.99$. Pore size distribution of the samples was determined using the Barret–Joyner–Halenda (BJH) method from the desorption data.

Scanning electron microscopy (SEM)–Transmission electron microscopy (TEM)

The morphology of the catalysts was studied using a JEOL JSM6510 LV scanning electron microscope coupled to xx-ActEnergy Dispersive Spectrometer (EDS) (Oxford Instruments) and a Philips CM20 high resolution transmission electron microscope (HRTEM).

Particle size determination

Secondary particle size (aggregates) measurements were conducted with a Shimadzu SALD-2300 laser diffraction particle size analyzer in dynamic light scattering mode (DLS). Prior to particle size measurements, aqueous suspensions of the studied materials were sonicated for 10 min using a sonicator probe (Hielscher Ultrasonics GmbH, UP50H).
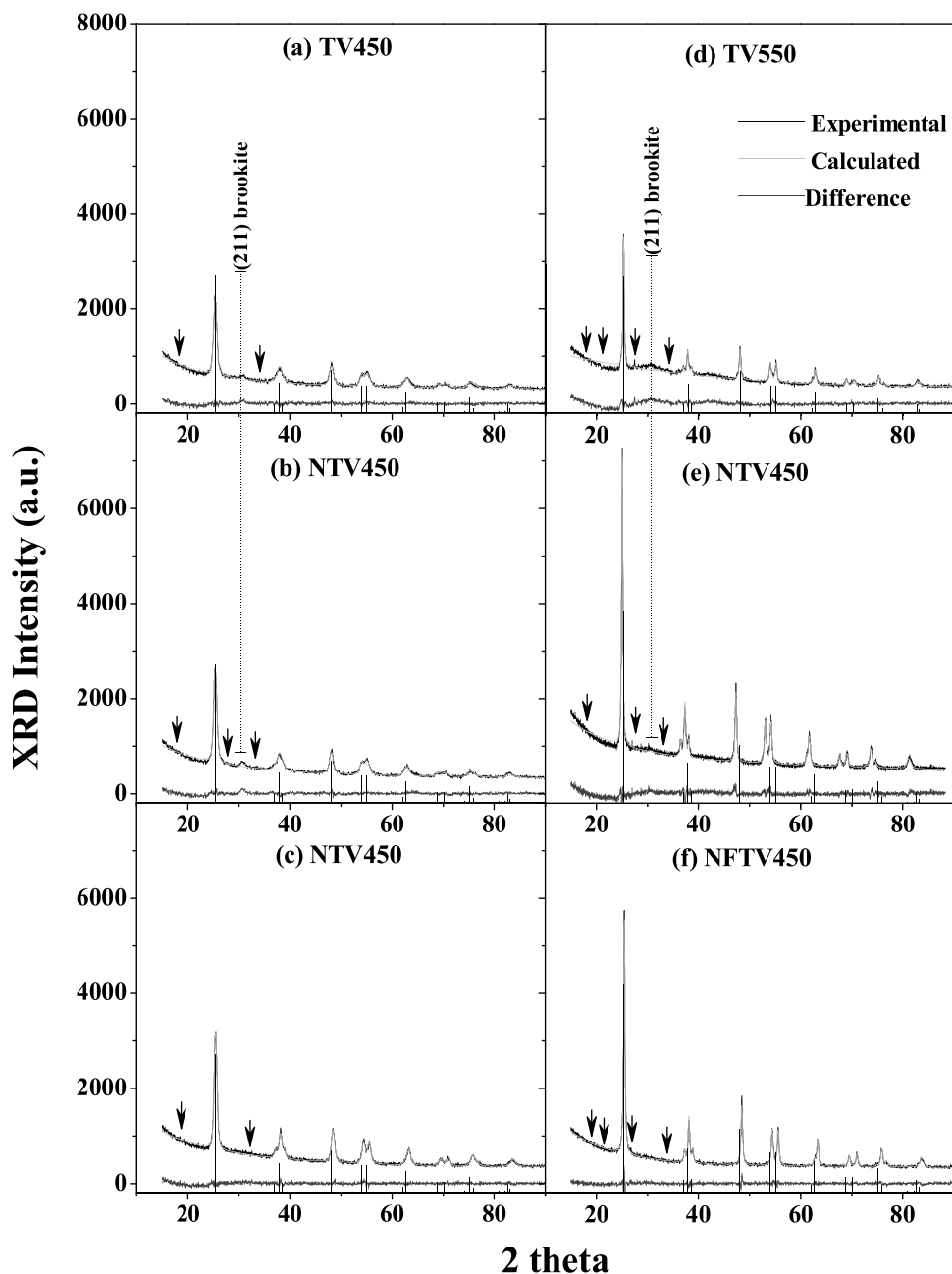

Fig. 1. X-ray diffractograms of all studied nanocomposite photocatalysts.

Photocatalytic experiments and analytical methods

Photocatalytic experiments were carried out in a solar simulator Atlas Suntest XLS+ (Germany) equipped with a xenon lamp (2.2 kW) jacketed with special glass filters restricting the transmission of wavelengths below 290 nm. The temperature of the sample was maintained at 20 °C using a tap water cooling circuit, preventing any heating of the suspension. An average irradiation intensity of 500 Wm^{-2} was maintained throughout the experiments and was measured by internal radiometer supplied by the manufacturer. Irradiation experiments were performed using a cylindrical 250 mL Duran® glass reactor with a flat flange lid with three necks containing 250 mL of aqueous solutions (0.05 mM Cr(VI) and 0.01 mM terephthalic acid). The pH of solutions was adjusted by H$_2$SO$_4$ at pH = 2 to obtain faster reduction kinetics of Cr(VI) as a result of: (a) enhanced adsorption of Cr(VI), since HCrO$_4^-$ ions are the dominant species at this pH; (b) avoiding precipitation of Cr(OH)$_3$ into the photocatalyst surface and (c) favorable thermodynamic driving force of electrons from the conduction band of the photocatalyst to Cr(VI) with pH's decreasing [37]. The solutions were mixed with the appropriate amount of catalyst and were magnetically stirred before and during the illumination. The suspensions were kept in the dark for 30 min prior to illumination to reach adsorption equilibrium on the catalyst surface. The adsorption percentages of Cr(VI) followed the trend: 2.5% for TV450, 4.1% for NTV450 and 5.5% for NFTV450. The adsorption percentages between the photocatalysts with the same heterostructure prepared at different calcination temperatures differed less than 1%. Control experiments in the absence of catalyst were also performed. In addition, experiments under N$_2$ and O$_2$ atmosphere were conducted by flushing the reactor with pure N$_2$ and O$_2$ for 30 min before the illumination and during the photocatalytic treatment. Aliquots (≈3 mL) were withdrawn from the reactor at different time intervals and were filtered through 0.45 μm (PVDF, HVLP) filters to remove catalyst's particles before further analysis.

The concentration of Cr(VI) was determined by the diphenyl-carbazide colorimetric method [38] at a wavelength of 540 nm using a UV–vis spectrophotometer (Jasco V-560). Relative errors lower than 5.5% were obtained in all cases.

Determination of •OH radicals by fluorescence measurements

The hydroxyl radical formation rate is determined using terephthalic acid (TA) (Sigma Aldrich, 98%), as a probe. Aqueous solution containing 2×10^{-3} M NaOH and 5×10^{-4} M TA was prepared and 20 mg of photocatalyst powder was suspended in the photocatalytic reactor and stirred for 30 min prior to UV–vis irradiation. Irradiation conditions were identical to that followed during the photocatalytic experiments. Using 310 nm as the excitation wavelength, the intensity of fluorescence peak at 425 nm, which is attributed to 2-hydroxyterephthalic acid (TAOH), was measured with a fluorescence spectrophotometer (Shimadzu RF-5300PC). The concentration of •OH radicals was estimated by a calibration curve plotting the fluorescence intensity of standard TAOH (TCI, >98%) aqueous solutions.

Results and discussion

Catalysts characterization

Textural properties

Fig. 1 shows the XRD patterns of all TV, NTV and NFTV samples. It is observed that all the diffraction peaks of samples could be
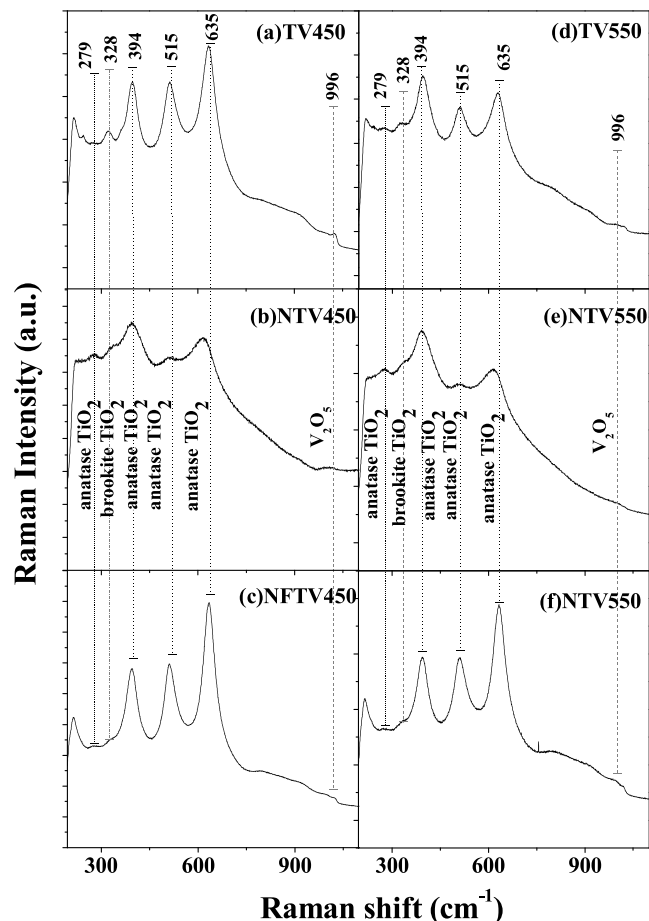

Fig. 2. Raman spectra of all studied nanocomposite photocatalysts.

Table 2
Results of XRD with Rietveld analysis of all studied nanocomposite photocatalysts.

Sample code name	Rietveld analysis						
	Crystal phase (%)	a	b	c	Unit cell volume (nm)	Crystal size (nm)	Strain (%)
	Anatase-JCPDS 21-1272 Tetragonal I41	3.7842	3.7842	9.5146	13.630	–	–
	Brookite JCPDS 29-1360 Orthorhombic Pbca	9.184	5.447	5.145	25.74		
TV450	Anatase/brookite (96/4)	3.8603	3.8603	9.6726	14.414	8.6 ± 0.2	0.470 ± 0.054
NTV450	Anatase/brookite (95/	3.7856	3.7856	9.4882	13.600	8.9 ± 0.1	0.206 ± 0.028
NFTV450	Anatase (100)	3.7532	3.7532	9.4142	13.250	9.6 ± 0.2	0.129 ± 0.022
TV550	Anatase/brookite (98/2)	3.7774	3.7774	9.4845	13.530	26.2 ± 2.6	0.282 ± 0.028
NTV550	Anatase/brookite (99/1)	3.8565	3.857	9.6861	14.410	28.1 ± 0.8	0.184 ± 0.012
NFTV550	Anatase (100)	3.7483	3.7483	9.4170	13.230	29.8 ± 18	0.082 ± 0.017

Table 3
Hydrodynamic particle size and textural characteristics (SSA, average pore diameter (D_{mean})) and band-gap energy (E_g) values of all studied photocatalysts.

Sample code name	Particle size Median (μm)	SSA ($m^2 g^{-1}$)	D_{mean} (nm)	E_g (eV)
TV450	0.326	80.2	6.8	2.79
NTV450	0.326	68.3	7.8	2.74
NFTV450	0.274	54.0	12.8	2.73
TV550	0.333	38.0	9.7	2.54
NTV550	0.322	28.8	12.4	2.57
NFTV550	0.339	28.5	19.0	2.71

readily indexed to the tetragonal phase of TiO$_2$ (JCPDS No. 01-084-1286). Traces (less than 5%) of brookite phase (TiO$_2$ JCPDS 29-1360) with orthorhombic P$_{bca}$ space group were observed in the case of TV and NTV samples in accordance with our previous reports [6,8] and denoted with dotted lines. As far as V$_2$O$_5$ phase, very small diffraction peaks are observed in all cases in the range of 15–40° 2theta as it is denoted with arrows. This may be attributed to the relatively low content and highly dispersed V$_2$O$_5$ in the nanocomposites, which was suggested [27] to be favorable for photocatalytic performance of catalysts.

Using anatase TiO$_2$ (JCPDS No. 01-084-1286) phase as starting model, a Rietveld refinement of the obtained XRD data with applicable software was performed based on the methodology reported elsewhere [39]. The average crystal size as well as the % strain values for anatase was calculated according to Williamson and Hull [40,41] method using the anatase phase reflections at 25.21° (1 0 1), 47.90° (2 0 0), 53.5° (1 0 5), 54.9° (2 1 1) and 61.8° (2 1 3). Calculated crystal lattice refinement values as well as crystallite size and % strain values for all samples are tabulated for comparison in Table 2. The cell parameters (Table 2) for all prepared solids show a small difference in comparison with the theoretical values of pure TiO$_2$ anatase phase. Crystal lattice distortion is caused by the doping process [2,6,9,42] and this is known to be important for absorption-edge shift toward the visible-light region. The calcination of the catalysts from 450 °C to 550 °C resulted in: [i] increase of crystallite size values; [ii] decrease

of % strain values and [iii] increased V$_2$O$_5$ crystallite sizes due to the faster growth in comparison to TiO$_2$ [43]. In other words, calcination leads to bigger crystallites with less lattice defects [44]. As it is known, small crystal size values [45,46] and higher lattice defects [47,48] are beneficial for the photocatalytic performance of the catalysts.

The Raman spectrum (Fig. 2) is characterized by the peaks located at around 279 cm^{-1}, 328 cm^{-1}, 394 m^{-1}, 515 cm^{-1}, 635 cm^{-1} and 996 cm^{-1}. The main and more intense peaks at 394 cm^{-1}, 515 cm^{-1}, 635 cm^{-1} as well as the broad peak at 279 cm^{-1} denoted with dotted lines in Fig. 2 correspond to anatase TiO$_2$ phase [49,50]. The broad peak at 996 cm^{-1} denoted with gray dashed line in Fig. 2 corresponds to V$_2$O$_5$ phase [51–54]. The peak at around 328 cm^{-1} denoted with the dashed dotted line in Fig. 2 appeared only in TV and NTV samples corresponds to brookite TiO$_2$ crystal phase [51]. Raman results are in full agreement with XRD results where broad or very small peaks were also detected for orthorhombic V$_2$O$_5$ crystal phase while traces of brookite TiO$_2$ were observed for TV and NTV samples.

The adsorption–desorption isotherms are shown in Fig. S1 while Table 3 lists the specific surface area (SSA) and the mean pore diameter (D_{mean}) for all TV, NTV and NFTV nanocomposite catalysts. As observed in Fig. S1, all nanocatalysts displayed a type IV adsorption isotherm with an H3 hysteresis loop type according to the IUPAC classification. From Fig. S1 and the results listed in Table 3, it is concluded that all prepared samples are typical mesoporous materials. For the nanocomposites calcined at 450 °C the SSA value ranged between 80.2 m^{2}g^{-1} for TV450 and 68.3 m^{2}g^{-1} for NTV450. Comparing the crystallite size values listed in Table 2 and SSA values listed in Table 3 it can be observed that SSA values decreased as the crystallinity of nanocomposites increased. Based on Fig. S1 and SSA, D_{mean} values (Table 3), it can be postulated that calcination at 550 °C decreases the surface area and increases the mean pore volume values for all nanocomposite catalysts. This result agrees with previous studies [44,55] reporting that calcination temperature increases crystallinity and particle size and thus decreases porosity.
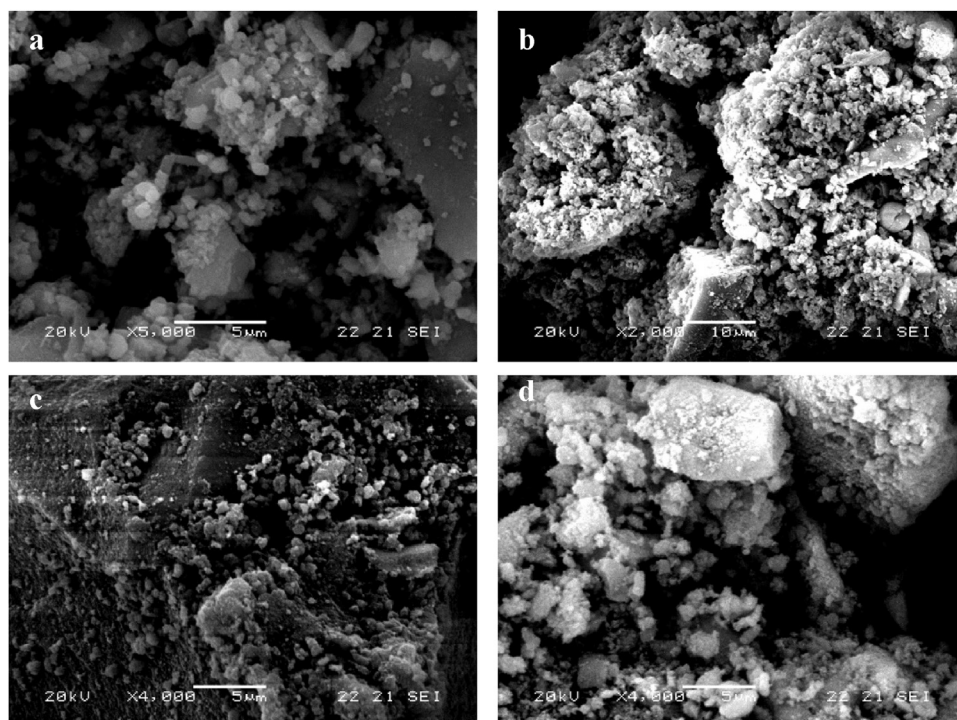

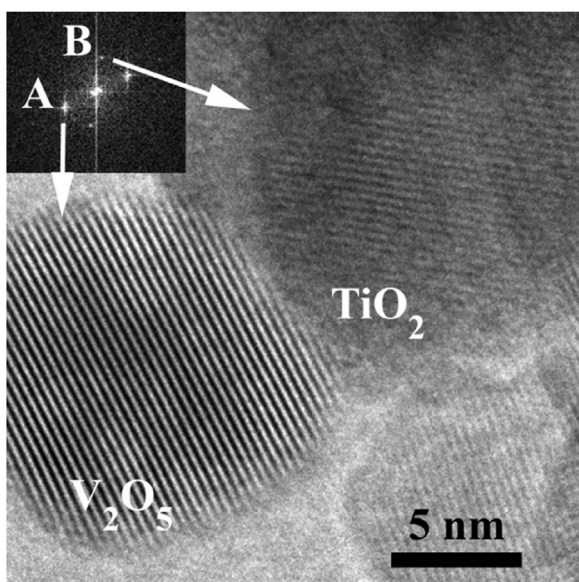**Fig. 3.** SEM images of (a) TV450, (b) NTV450, (c) NFTV450 and (d) NFTV550 catalysts.
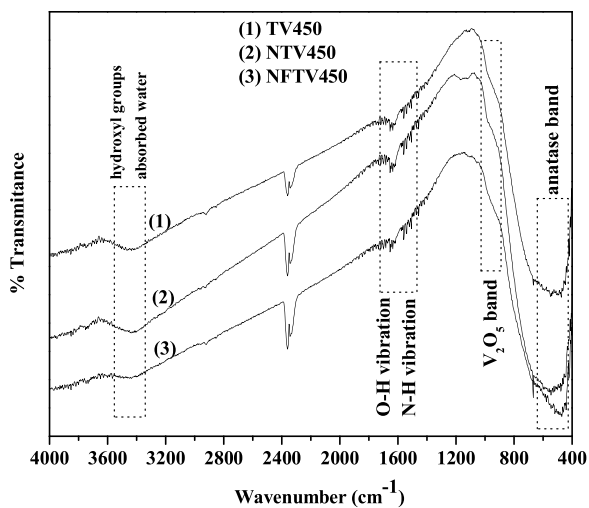
Fig. 4. HRTEM image of TV450 catalyst.

Fig. 5. FT-IR spectra of all studied nanocomposite photocatalysts calcined at 450 °C.

Fig. 6. (a) UV–vis diffuse-reflectance spectra; (b) first derivative plots of UV–vis DRS plots and (c) Kübelka–Münk plots of all tested nanocomposite photocatalysts.

SEM images for TV450, NTV450 and NFTV450 samples are shown in Fig. 3(a–c) and in Fig. 3d for NFTV550 sample. It is illustrated that all samples are composites of larger particles with 5–20 μm diameter and smaller particles with 100–200 nm diameter. Smaller diameter particles are dispersed over the surface of the larger particles while no aggregates of smaller particles was obtained [54]. Therefore, this result is in accordance with XRD pattern of composites, in which very small peaks of V_2O_5 was observed [6]. For confirming further the heterostructure of the prepared catalysts, high resolution transmission electron microscopy (HRTEM) was performed. A HRTEM image of TV450 catalyst can be seen in Fig. 4 where the lattice fringes of two nanoparticles in contact are depicted. The associated fast Fourier transform (FFT) is shown in the inset. The spot labeled as A originates from the lattice fringes of the lower nanoparticle and has a d-spacing of 0.341 nm corresponding to (110) V_2O_5 planes, while the spot labeled as B originates from the lattice fringes of the upper-right nanoparticle and has a d-spacing of 0.352 nm corresponding to (101) anatase planes.

Finally, Table 3 summarizes particle size values calculated by PLS in aqueous suspensions of the catalysts after sonication for
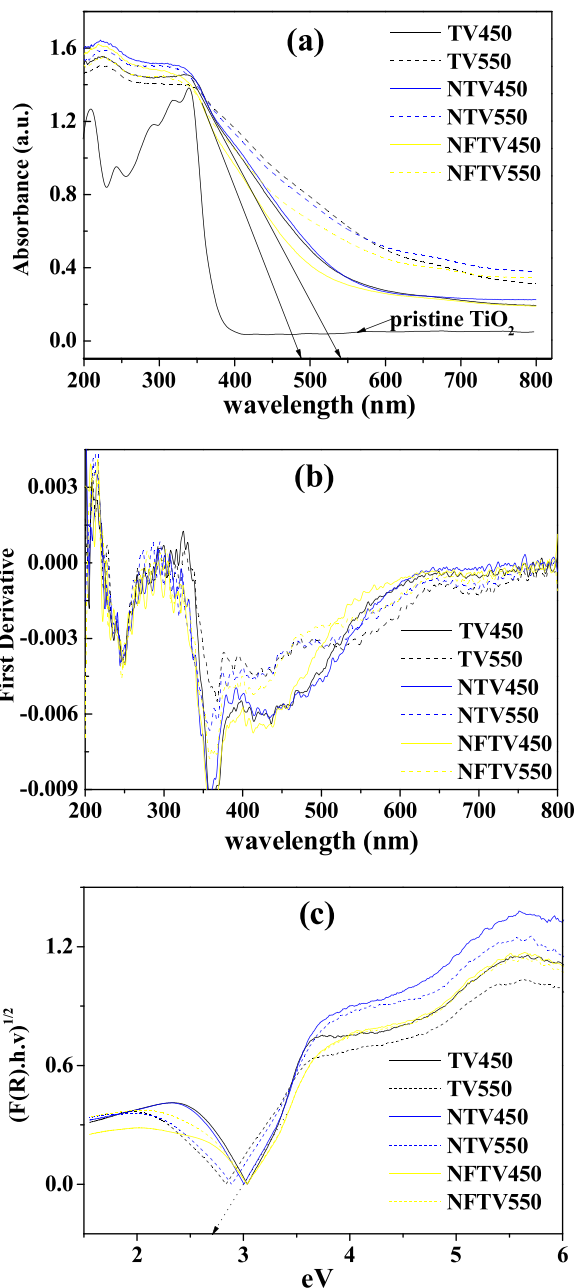
10 min. Similar agglomeration for TV and NFTV catalyst particles was observed while a lower extent was recorded for NFTV450 catalyst.

FT-IR results

Fig. 5 shows the FT-IR spectra in the range 450–4000 cm^{-1} for TV450, NTV450 and NFTV450 samples. All samples have similar FT-IR spectra, indicating the success of preparation method to achieve similar dispersions in all cases of TV, NTV and NFTV samples. The broad band at 3400 cm^{-1} was observed in the spectra of all samples ascribed to surface hydroxyl groups and adsorbed water molecules [56,57]. The intensity of this broad peak follows the trend NTV450 > TV450 > NFTV450. The peak at around ~1630 cm^{-1} corresponds to bending vibrations of O—H and N—H for N-doped samples [57,58]. The absorption peak at

Table 4
Summary of kinetic parameters for Cr(VI) reduction in binary (Cr(VI)-TA) and single (Cr(VI)) (in parenthesis) systems and $^{\bullet}$OH radicals formation under UV–vis irradiation.

Photocatalyst	Cr(VI) reduction			$^{\bullet}$OH formation	
	k (min^{-1})	$t_{1/2}$ (min)	R^2	k (μmol min^{-1})	R^2
TV 450	0.0157 (0.0141)	44.1 (49.2)	0.9705 (0.9619)	0.0054	0.9800
TV 550	0.0084	82.5	0.9810	0.0032	0.9404
NTV 450	0.0149 (0.0137)	46.5 (50.0)	0.9493 (0.9937)	0.0059	0.9487
NTV 550	0.0064	108.3	0.9976	0.0025	0.9937
NFTV 450	0.0087 (0.0080)	79.6 (86.6)	0.9823 (0.9942)	0.0110	0.9900
NFTV 550	0.0061	113.6	0.9937	0.0074	0.9855
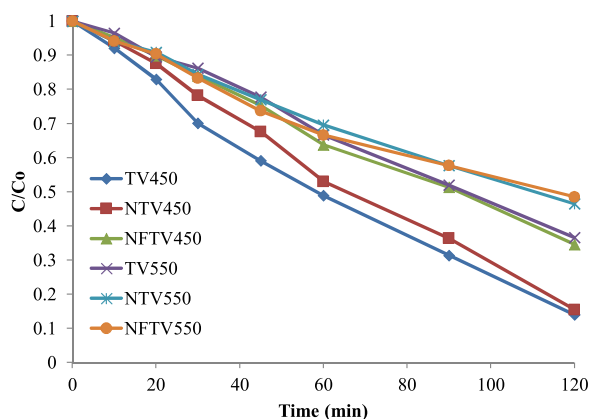
Fig. 7. Photocatalytic kinetics of Cr(VI) reduction for the studied catalysts (experimental conditions: [catalyst] = 200 mg L^{-1}; [Cr(VI)] = 0.05 mM; [terephthalic acid] = 0.01 mM; I = 500 Wm^{-2}).

2345 cm^{-1} is characteristic of surface adsorbed CO_2 [56,59]. The Ti—O—Ti bending vibration at 420–650 cm^{-1} confirms the formation of anatase TiO_2 [24] in consistency with XRD results. The broad shoulder peak of V_2O_5 band at $\sim$981 cm^{-1} [56] in all samples implies the low content and highly dispersed state of V_2O_5 crystallites in accordance with XRD results.

UV–vis diffuse reflectance spectra (DRS)

Fig. 6a shows typical UV–vis absorption spectra for all TV, NTV and NFTV nanocomposite catalysts. As it is shown in Fig. 6a the adsorption edge of pristine TiO_2 sample appeared at 382 nm [6]. In the presence of V_2O_5, all samples exhibit visible light absorption with absorption edges clearly shifted to $\sim$480–540 nm. In Fig. 6b the first derivative plots of all tested photocatalysts are shown depicting better the absorption bands in the visible light region. For catalysts calcined at 550 °C three main bands can be observed; the first one was observed around 340–400 nm, the second one around 420–550 nm and the third one above 600 nm. For the catalysts calcined at 450 °C the second band it is better observed than catalysts calcined at 550 °C. In accordance with previous report [49], the absorption band around 420–550 nm was correlated to the decrease of band gap energy by the addition of V_2O_5 species. On the other hand, the band around 650–750 nm observed for the catalysts calcined at 550 °C is attributed to the polymeric vanadium oxide species formed on the surface of the TiO_2 [49,58,60,69].

The E_g values for all TV, NTV and NFTV nanocomposite catalysts calculated from the Kübelka–Münk plots (Fig. 6c) are listed in Table 3. It is observed that: [i] E_g values of all photocatalysts calcined at 450 °C follow the trend TV > NTV > NFTV and [ii] E_g values of all photocatalysts calcined at 550 °C follow the trend NFTV > NTV > TV. The results for 450 °C calcined photocatalysts are in accordance with our previous reports [6–8]. It is well known [2] that N doping creates new states above conduction band of TiO_2 and thus shortening the band gap. Moreover, N-doping in the presence of F$^-$ ions incorporates N atoms deeper in the lattice and creates Ti^{3+} lattice states below reduction band of TiO_2 [6,8], thus narrowing more the band gap. For the samples calcined at 550 °C the trend in E_g values is opposite to that expected for N and N,F-co-doped samples. In other words, it could be stated that the increase of calcination temperature causes a decrease to the E_g values, mainly for the TV550 samples due to the increased growth of V_2O_5 phase.

Photocatalytic activity

Photocatalytic reduction of Cr(VI)

Firstly, preliminary experiments under simulated solar light in the absence of catalysts and using the same initial concentration of substrates were carried out. The reduction of Cr(VI) followed slow first-order kinetics (R^2 = 0.9709) with a reaction constant k = 0.0016 min^{-1} and a half-life $t_{1/2}$ = 433.1 min. Thus, the contribution of the photolytic process in the overall photocatalytic kinetics was minor. Subsequently, photocatalysis experiments in single (Cr(VI)) and binary (Cr(VI) and TA) systems were performed for catalysts calcined at 450 °C and the apparent first-order kinetic constants for Cr(VI) reduction ($k_{Cr(VI)}$) are listed in Table 4. In accordance with the well documented enhanced photoreduction of a metal ion in the presence of organic compounds such as carboxylic acids and phenols [33], a synergistic effect between TA and Cr (VI) was observed under all tested irradiation systems due to a better separation of photogenerated charge carriers. The photocatalytic kinetics in binary systems for all prepared catalysts (calcined both

Fig. 8. Proposed mechanism for the photocatalytic reduction of Cr(VI) and photocatalytic oxidation of organic compounds by $^{\bullet}$OH radical generation for the studied V_2O_5/TiO_2, V_2O_5/N-TiO_2 and V_2O_5/N,F-TiO_2 photocatalysts.
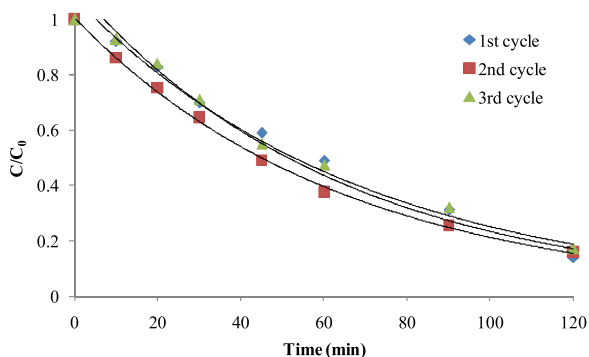
Fig. 9. Reusability performance of TV450 catalyst for three consecutive catalytic cycles (experimental conditions: [catalyst] = 200 mg L^{-1}; [Cr(VI)] = 0.05 mM; [terephthalic acid] = 0.01 mM; I = 500 Wm^{-2}).

in 450 °C and 550 °C) are shown in Fig. 7. Based on the values of first-order kinetic constants (Table 4), it can be concluded that: [i] photocatalysts calcined at 450 °C exhibit higher photocatalytic rates for Cr(VI) reduction than photocatalysts calcined at 550 °C and [ii] photocatalytic reduction of Cr(VI) follows the sequence TV450 > NTV450 > NFTV450 for catalysts calcined at 450 °C while the sequence TV550 > NTV550 = NFTV550 is followed for catalysts calcined at 550 °C. The lower activity of photocatalysts calcined at 550 °C can be explained considering the much higher crystallite sizes, lower defects and lower SSA values than photocatalysts calcined at 450 °C. The previously stated catalytic activity sequence can be explained taking into account the photocatalytic mechanism of TiO$_2$/V$_2$O$_5$ heterostructures [49,51,61,62], as shown in Fig. 8, and the e$^-$/h$^+$ dynamics and properties of N-TiO$_2$ and N-F-TiO$_2$ catalysts as previously studied [6,63–65]. More specifically, TiO$_2$/V$_2$O$_5$ heterostructures are beneficial for the separation of the photogenerated charge pairs (e$^-$/h$^+$) through interfacial e$^-$ transfer from the conduction band of V$_2$O$_5$ to the conduction band of TiO$_2$ and h$^+$ transfer from the valence band of TiO$_2$ to the valence band of V$_2$O$_5$. As a result, electrons assembled in the CB of TiO$_2$ phase while holes assembled in the V$_2$O$_5$ phase. As far as N-TiO$_2$ and N-F-TiO$_2$ phases, they presented the following main aspects: [i] N-doping creates new states above conduction band of TiO$_2$, thus shortening the band gap; [ii] N-F-TiO$_2$ generate exclusively lattice Ti(III) electrons due to the charge compensation between Ti^{4+} and F-; [iii] N-TiO$_2$ generates more surface Ti(III) electrons; [iv] lattice Ti(III) electrons in N-F-TiO$_2$ materials are situated deeper and are thermodynamically less efficient in Cr(VI) reduction than surface Ti(III) electrons [6,57]. It is suggested that in NTV and NFTV catalysts the surface and lattice Ti(III) ions scavenge in a significant extent the electrons transferred from V$_2$O$_5$ to TiO$_2$ conduction band, thus decreasing the free surfacial electrons which are available for Cr(VI) reduction. The scavenging of electrons is higher in NFTV sample than NTV one where the Ti(III) are localized deeper in the lattice. Thus, the available surface electrons for Cr(VI) reduction follows the trend TV > NTV > NFTV which is the same trend with the observed photocatalytic activity. In addition, similar photocatalytic reduction kinetics of Cr(VI) were observed under N$_2$ (k = 0.0160 min^{-1}; t$_{1/2}$ = 43.3 min; R^2 = 0.9959) and O$_2$ (k = 0.0158 min^{-1}; t$_{1/2}$ = 43.6 min; R^2 = 0.9906) atmosphere showing that Cr (VI) is reduced directly by photogenerated electrons while O$_2$ competition is minor.

Finally, in order to investigate the stability and recyclability of the prepared photocatalysts the photocatalytic kinetics of Cr(VI) reduction for three consecutive cycles were investigated for the most efficient catalyst TV450. According to the experimental results (Fig. 9) quite similar kinetic constants have been determined for the first, second and third catalytic cycle, i.e. 0.0157 min^{-1}, 0.0155 min^{-1}
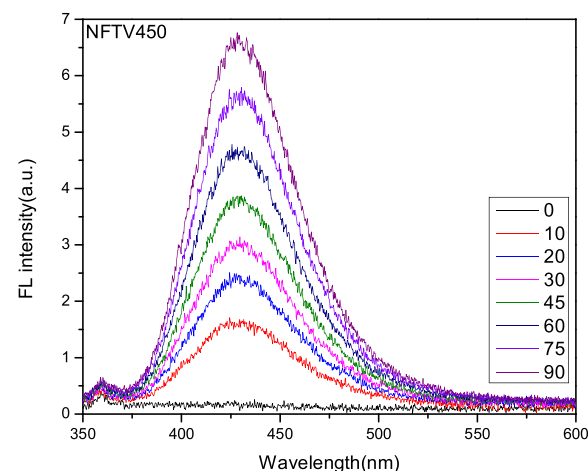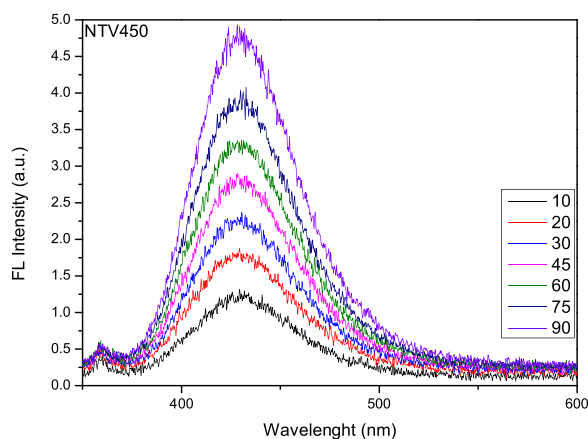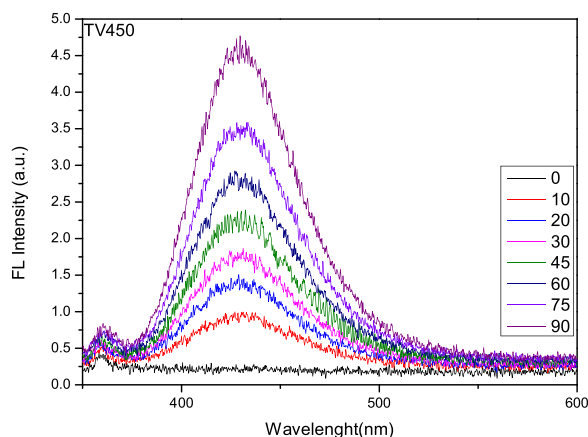

Fig. 10. Fluorescence spectra of OHTA formation for TV450, NTV450, NFTV450 catalysts.

and 0.0145 min^{-1}, respectively. A marginal loss of less than 10% of its catalytic performance was recorded after the third cycle indicating thus a good recyclability of the catalyst.

•OH radical generation

The photocatalytic activity of the prepared catalysts toward the oxidation of organic compounds was estimated by ·OH radical
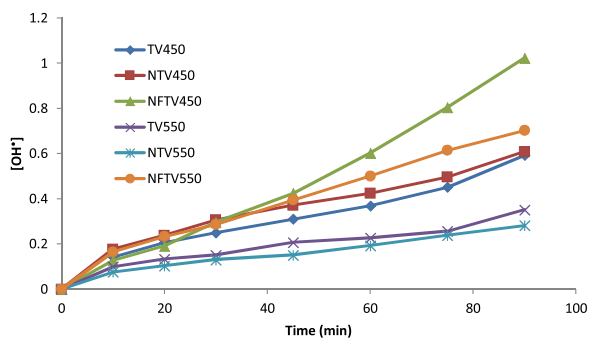
Fig. 11. Kinetics of •OH formation based on OHTA fluorescence measurements.

generation using terephthalic acid in alkaline solution as a probe. Figs. 10 and S2 show the fluorescence spectra of the generated hydroxy-terephthalic acid recorded at different time intervals for catalysts calcined at 450 °C and 550 °C, respectively. The evolution of the fluorescence intensity versus the irradiation time for all catalysts is also shown in Fig. 11. Based on Figs. 10 and 11 the OH generation capability of the prepared catalysts followed the trend NFTV450 > NTV450 > TV450   and   NFTV550 > TV550 = NTV550 while all catalysts calcined at 450 °C produce more radicals than the corresponding catalysts calcined at 550 °C. In comparison with the photocatalytic reduction of Cr(VI) the same activity was observed regarding the effect of calcination temperature while the inverse trend was observed among catalysts prepared at the same calcinations temperature. Similarly to Cr(VI) photocatalytic reduction, the better performance for the catalysts prepared at 450 °C can be attributed to the lower crystallite sizes, higher defects and SSA values and better exploitation of visible light absorption. The observed sequence for the catalysts prepared at the same calcination temperature can be explained considering the following aspects: [i] V_2O_5 loading increased the photocatalytic activity due to the increase Brønsted acidity that helps to generate surface hydroxyl radicals [66]; [ii] F⁻ increase the surface acidity of the catalyst and the adsorption of organic molecules and OH⁻ ions generating more free •OH radicals at the solution-catalyst interface which are more reactive compared to surface-bound •OH radicals in undoped TiO_2 and N-TiO_2 [67–69]; [iii] Ti(III) sites enhances the adsorption of water to produce more hydroxyl radicals [49]. As a result more radicals OH radicals are generated for the NFTV catalysts in consistency with the observed results.

Conclusions

In the present work the successful preparation via a simple impregnation method of V_2O_5 supported on TiO_2, N-TiO_2 and N,F-TiO_2 photocatalysts with mesoporous structure was presented. The formation of anatase was observed as the main TiO_2 crystal phase in all cases. The increase of calcination temperature from 450 °C to 550 °C lead to increased crystallite sizes and decreased lattice strain values, specific surface areas and pore volume for all photocatalysts. V_2O_5 coupling with TiO_2 extended the absorption edge to the visible light region in all cases while the absorption edge above 600 nm attributed to the polymeric vanadium oxide species formed on the surface of the TiO_2. Photocatalysts calcined at 450 °C exhibited higher Cr(VI) reduction and •OH radicals photogeneration rates than photocatalysts calcined at 550 °C due to the lower crystallite size and higher strain and SSA values. NTV and NFTV samples exhibited lower Cr(VI) reduction rates and higher photogenerated •OH values than TV ones. Regarding the reduction efficiency of the catalysts it was suggested that the formation of surface and lattice Ti(III) ions act as scavengers for the

electrons transferred from V_2O_5 to TiO_2 conduction band and thus decrease the free surfacial electrons available for Cr(VI) reduction. For OH radical photogeneration it was suggested that F⁻ increase the surface acidity of the NFTV catalyst and the adsorption of organic substrates while Ti(III) sites enhances the adsorption of water to produce more hydroxyl radicals on NTV and NFTV samples.

Appendix A. Supplementary data

Supplementary data associated with this article can be found, in the online version, at https://doi.org/10.1016/j.jiec.2018.05.008.

References

[1] I.K. Konstantinou, T.A. Albanis, Appl. Catal. B: Environ. 42 (4) (2003) 319.
[2] L.G. Devi, R. Kavitha, Appl. Catal. B: Environ. 140–141 (2013) 559.
[3] M. Pelaez, N.T. Nolan, S.C. Pillai, M.K. Seery, P. Falaras, A.G. Kontos, P.S.M. Dunlop, J.W.J. Hamilton, J.A. Byrne, K. O'Shea, M.H. Entezari, D.D. Dionysiou, Appl. Catal. B: Environ. 125 (2012) 331.
[4] M.A. Rauf, M.A. Meetani, S. Hisaindee, Desalination 276 (1–3) (2011) 13.
[5] M.V. Dozzi, E. Selli, J. Photochem. Photobiol. C: Photochem. Rev. 14 (1) (2013) 13.
[6] A.E. Giannakas, E. Seristatidou, Y. Deligiannakis, I. Konstantinou, Appl. Catal. B: Environ. 132–133 (2013) 460.
[7] A.E. Giannakas, M. Antonopoulou, Y. Deligiannakis, I. Konstantinou, Appl. Catal. B: Environ. 140–141 (2013) 636.
[8] A.E. Giannakas, M. Antonopoulou, C. Daikopoulos, Y. Deligiannakis, I. Konstantinou, Appl. Catal. B: Environ. 184 (2016) 44.
[9] V. Makrigianni, A. Giannakas, C. Daikopoulos, Y. Deligiannakis, I. Konstantinou, Appl. Catal. B: Environ. 174–175 (2015) 244.
[10] M. Antonopoulou, P. Karagianni, A. Giannakas, V. Makrigianni, E. Mouzourakis, Y. Deligiannakis, I. Konstantinou, Catal. Today 280 (2017) 114.
[11] J.A. Mendoza, D.H. Lee, J.-H. Kang, Chemosphere 182 (2017) 539.
[12] J. Xu, Y. Ao, D. Fu, C. Yuan, Appl. Surf. Sci. 255 (2008) 2365.
[13] J. Kim, M. Kang, Int. J. Hydrogen Energy 37 (10) (2012) 8249.
[14] H. Yang, J. Tian, Y. Bo, Y. Zhou, X. Wang, H. Cui, J. Colloid Interface Sci. 487 (2017) 258.
[15] I.A. Perales-Martínez, V. Rodríguez-González, S.W. Lee, S. Obregón, J. Photochem. Photobiol. A: Chem. 299 (2015) 152.
[16] L. Xie, P. Liu, Z. Zheng, S. Weng, J. Huang, Appl. Catal. B: Environ. 184 (2016) 347.
[17] J. Wang, X. Wang, X. Liu, T. Zhu, Y. Guo, H. Qi, Catal. Today 241 (PA) (2015) 92.
[18] H. Jung, E. Park, M. Kim, J. Jurng, Waste Manag. 61 (2017) 283.
[19] H. Zhao, S. Bennici, J. Cai, J. Shen, A. Auroux, Catal. Today 152 (1–4) (2010) 70.
[20] T. Mongkhonsi, L. Kershenbaum, Appl. Catal. A Gen. 170 (1998) 33.
[21] D. Ye, R. Qu, H. Song, X. Gao, Z. Luo, M. Ni, K. Cen, Chem. Eng. J. 283 (2016) 846.
[22] X. Zhou, X. Chen, Q. Bi, X. Luo, L. Sun, Z. Liu, Ceram. Int. 43 (15) (2017) 12689.
[23] A.W. Lothongkum, P. Sethapokin, P. Ouraipryvan, J. Ind. Eng. Chem. 25 (2014) 288.
[24] E. Sinirtas, M. Isleyen, G.S.P. Soylu, Cuihua Xuebao/Chin. J. Catal. 37 (4) (2016) 607.
[25] M. Isleyen, E.S. Ilkme, G.S.P. Soylu, Korean J. Chem. Eng. 34 (6) (2017) 1786.
[26] X.H. Yang, H.T. Fu, X.Z. An, X.C. Jiang, A.B. Yu, RSC Adv. 6 (2016) 34103.
[27] L. Xie, P. Liu, Z. Zheng, S. Weng, J. Huang, Appl. Catal. B: Environ. 184 (2016) 347.
[28] D. Pradhan, L.B. Sukla, M. Sawyer, P.K.S.M. Rahman, J. Ind. Eng. Chem. 55 (2017) 1.
[29] B. Li, Y. Wang, F. Tian, G. Li, Y. Song, J. Ind. Eng. Chem. 54 (2017) 398.
[30] Z. Hasan, J. Cho, J. Rinklebe, Y.S. Ok, H. Song, J. Ind. Eng. Chem. 52 (2017) 331.
[31] S. Park, R. Selvaraj, M.A. Meetani, Y. Kim, J. Ind. Eng. Chem. 45 (2017) 206.
[32] M.H. Dehghani, B. Heibati, A. Asadi, I. Tyagi, V.K. Gupta, J. Ind. Eng. Chem. 33 (2016) 197.
[33] M. Antonopoulou, A. Giannakas, I. Konstantinou, Int. J. Photoenergy (2012) 2012.
[34] C.G. Skoutelis, M. Antonopoulou, A.E. Giannakas, Y. Deligiannakis, I.K. Konstantinou, J. Adv. Oxid. Technol. 17 (2) (2014).
[35] R. López, R. Gómez, J. Sol Gel Sci. Technol. 61 (1) (2012) 1.
[36] B. Wang, G. Zhang, X. Leng, Z. Sun, S. Zheng, J. Hazard. Mater. 285 (2015) 212.
[37] M. Antonopoulou, I. Chondrodimou, F. Bairamis, A. Giannakas, I. Konstantinou, Environ. Sci. Pollut. Res. 24 (2017) 1063.

[38] N. Wang, Y. Xu, L. Zhu, X. Shen, H.J. Tang, Photochem. Photobiol. A: Chem. 201 (2009) 121.

[39] H. Rietveld, Acta Crystallogr. 22 (1967) 151.

[40] W.H.G. Williamson, Acta Metall. 1 (1953) 22.

[41] W. Hall, Proc. Phys. Soc. A 62 (1949) 741.

[42] A. Koltsakidou, M. Antonopoulou, E. Evgenidou, I. Konstantinou, A.E. Giannakas, M. Papadaki, D. Bikiaris, D.A. Lambropoulou, Sci. Total Environ. 578 (2017) 257.

[43] Q. Su, J. Zhang, Y. Wang, M. Yu, C. Zhu, W. Lan, X. Liu, J. Phys. Chem. Solids 74 (10) (2013) 1475.

[44] Y.F. Chen, C.Y. Lee, M.Y. Yeng, H.T. Chiu, J. Cryst. Growth 247 (3–4) (2003) 363.

[45] Z.X.L. Yue, M. Shui, Acta Chim. Sin. 57 (1999) 1219.

[46] W. Choi, A. Termin, M.R. Hoffmann, J. Phys. Chem. 98 (51) (1994) 13669.

[47] X. Wang, M. Shui, R. Li, Y. Song, Mater. Res. Bull. 43 (8–9) (2008) 2476.

[48] M. Gurulakshmi, M. Selvaraj, A. Selvamani, P. Vijayan, N.R. Sasi Rekha, K. Shanthi, Appl. Catal. A Gen. 449 (2012) 31.

[49] D. Lu, B. Zhao, P. Fang, S. Zhai, D. Li, Z. Chen, W. Wu, W. Chai, Y. Wu, N. Qi, Appl. Surf. Sci. 359 (2015) 435.

[50] Y. Wang, Y.R. Su, L. Qiao, L.X. Liu, Q. Su, C.Q. Zhu, X.Q. Liu, Nanotechnology 22 (22) (2011) 225702.

[51] Z. Wu, F. Dong, Y. Liu, H. Wang, Catal. Commun. 11 (2) (2009) 82.

[52] F. Dong, Y. Sun, M. Fu, Int. J. Photoenergy (2012) 2012, doi:http://dx.doi.org/10.1155/2012/569716.

[53] R.K. Jain, A. Khanna, Opt. — Int. J. Light Electron Opt. 144 (2017) 271.

[54] M. Takeshi, N. Kaori, E. Watanabec, T. Hiroshi, Mater. Sci. 658 (2010) 495.

[55] W. Cha, S. Chin, E. Park, S.T. Yun, J. Jurng, Appl. Catal. B: Environ. 140–141 (2013) 708.

[56] J. Gardy, A. Hassanpour, X. Lai, M.H. Ahmed, M. Rehan, Appl. Catal. B: Environ. 207 (2017) 297.

[57] G. Yang, Z. Jiang, H. Shi, T. Xiao, Z. Yan, J. Mater. Chem. 20 (25) (2010) 5301.

[58] J. Senthilnathan, L. Philip, Chem. Eng. J. 161 (1–2) (2010) 83.

[59] S. Higashimoto, W. Tanihata, Y. Nakagawa, M. Azuma, H. Ohue, Y. Sakata, Appl. Catal. A Gen. 340 (1) (2008) 98.

[60] X. Zhou, J. Wu, Q. Li, Y. Qi, Z. Ji, P. He, X. Qi, P. Sheng, Q. Li, J. Ren, Chem. Eng. J. 330 (2017) 294.

[61] S. Martha, D.P. Das, N. Biswal, K.M. Parida, J. Mater. Chem. 22 (21) (2012) 10695.

[62] L. Xie, P. Liu, Z. Zheng, S. Weng, J. Huang, Appl. Catal. B: Environ. 184 (2016) 347.

[63] A.E. Giannakas, M. Antonopoulou, J. Papavasiliou, Y. Deligiannakis, I. Konstantinou, J. Photochem. Photobiol. A: Chem. 349 (2017) 25.

[64] C.P. Kumar, N.O. Gopal, T.C. Wang, M.-S. Wong, S.C. Ke, J. Phys. Chem. B 110 (2006) 5223.

[65] C. Di Valentin, E. Finazzi, G. Pacchioni, A. Selloni, S. Livraghi, A.M. Czoska, M.C. Paganini, E. Giamello, Chem. Mater. 20 (11) (2008) 3706.

[66] C.-H. Lin, H. Bai, Appl. Catal. B: Environ. 42 (3) (2003) 279.

[67] E.M. Bayan, T.G. Lupeiko, E.V. Kolupaeva, L.E. Pustovaya, A.G. Fedorenko, 193 (2017) 17.

[68] C. Minero, G. Mariella, V. Maurino, E. Pelizzetti, Langmuir 16 (6) (2000) 2632.

[69] E.M. Samsudin, S.B. Abd Hamid, Appl. Surf. Sci. 391 (2017) 326.